Characterization of a Continuous CO_2 Laser–Welded Fe-Cu Dissimilar Couple

GANDHAM PHANIKUMAR, SAMBANDAM MANJINI, PRADIP DUTTA,
JYOTIRMOY MAZUMDER, and KAMANIO CHATTOPADHYAY

Continuous CO_2 laser welding of an Fe-Cu dissimilar couple in a butt-weld geometry at different process conditions is studied. The process conditions are varied to identify and characterize the microstructural features that are independent of the welding mode. The study presents a characterization of the microstructure and mechanical properties of the welds. Detailed microstructural analysis of the weld/base-metal interface shows features that are different on the two sides of the weld. The iron side can grow into the weld with a local change in length scale, whereas the interface on the copper side indicates a barrier to growth. The interface is jagged, and a banded microstructure consisting of iron-rich layers could be observed next to the weld/Cu interface. The observations suggest that solidification initiates inside the melt, where iron and copper are mixed due to convective flow. The transmission electron microscopy (TEM) of the weld region also indicates the occasional presence of droplets of iron and copper. The microstructural observations are rationalized using arguments drawn from a thermodynamic analysis of the Fe-Cu system.

I. INTRODUCTION

ALTHOUGH the welding of metals and alloys is a mature subject,[1,2] dissimilar welding represents a major scientific and technical challenge. Emerging new technologies increasingly require dissimilar metals and alloys to be joined. Dissimilar welding processes involving electromagnetic fields have the possibility of beam deflection[3,4,5] due to several electromagnetic effects. This leads to missed joints in dissimilar couples such as Ni-Cu.[5,6] Laser processing is free of electromagnetic fields and is, thus, suitable for welding dissimilar couples. With flexibility in the power intensity, power distribution, and scanning velocity, laser welding is emerging as a major joining process.

The microstructures of laser-welded similar metals/alloys are reasonably well characterized.[1,2,7–9] However, there exist relatively fewer studies on the nature of weldments during fusion welding of dissimilar metals. A recent review by Sun and Ion[10] summarizes the studies on dissimilar metals. The two books by Steen[1] and Duley[2] also provide several references to this subject. Studies on dissimilar welds involving binary couples of pure metals are few,[11–14] and most of the literature concerns joining dissimilar alloys.[2,10,15–17] Few computational studies involving fluid flow, aimed at providing an understanding of the physical processes that influence the microstructure development during fusion welding of dissimilar metals, also can be found in recent times.[18–21]

Studies on dissimilar welding of pure binary couples will not only simplify the system for thermodynamic analysis, but also will provide experimental data to compare with computational studies. The difference between the physical properties of the two metals to be welded leads to an asymmetry in heat and fluid flow and leads to the development of unique features in the weld microstructure.[17] This, in turn, influences the integrity and mechanical properties of the weldments. A basic understanding of the evolution of microstructure during laser welding of dissimilar metals involves insight into the physical processes that take place during welding, the phase evolution from an inhomogeneous melt, and issues such as the growth of base metals into an alloy melt of different composition.

Iron and copper have large differences in physical properties and are, therefore, suitable for dissimilar laser welding studies. Further, iron- and copper-based alloys are common in structural applications and are of importance to the industry. However, couples of these two classes of alloys yield unsatisfactory joints during fusion welding. Understanding the microstructural features that arise during fusion welding will also be important to assess the possibility of using the two alloys in a dissimilar weld.

The phase diagram of iron and copper[22] is shown in Figure 1. The binary system of iron and copper contains a peritectic reaction in the iron-rich side and immiscibility in the solid state. Due to the flat liquidus, the existence of a metastable liquid-phase immiscibility in undercooled melts is expected and experimentally confirmed in this system.[23–26] Undercooled Fe-Cu liquid separates into droplets of iron and copper. Microstructural analysis of Fe-Cu alloys solidified at different cooling rates[26] indicates that liquid-phase separation is a common feature in most rapid solidification processes involving iron and copper. Studies on laser surface alloying of iron with copper suggest that this miscibility gap can be accessed easily.[27] The laser-alloyed regions are also characterized by a cellular microstructure with enhanced hardness. Microstructural features during welding of copper with iron filler wire also suggest similar features.[28] Thus, Fe-Cu forms a suitable system for a detailed study for the understanding of dissimilar welding.

GANDHAM PHANIKUMAR, Assistant Professor, Department of Metallurgical and Materials Engineering, Indian Institute of Technology Madras, Chennai 600036, India. Contact e-mail: gphani@iitm.ac.in SAMBANDAM MANJINI is with Jindal Vijaynagar Steel Limited, Bellary, 583275, India. PRADIP DUTTA, Associate Professor, and KAMANIO CHATTOPADHYAY, Professor and Chairman, are with the Department of Metallurgy, Indian Institute of Science, Bangalore 560012, India. JYOTIRMOY MAZUMDER, Robert H. Lurie Professor of Engineering, is with the Mechanical Engineering Department, University of Michigan, Ann Arbor, MI 48108.

Manuscript submitted May 25, 2004.

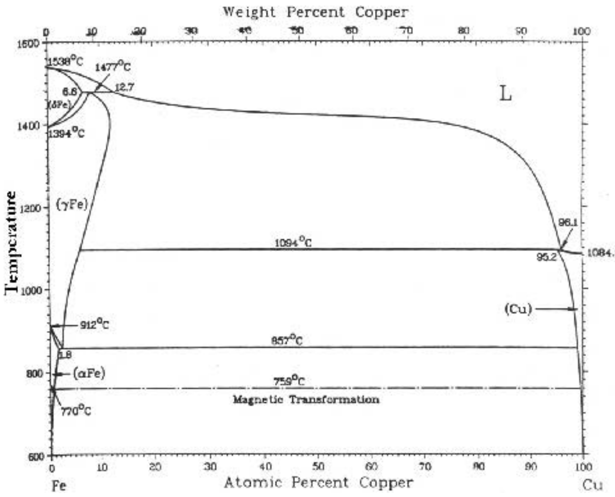

Fig. 1—Phase diagram of iron-copper.[22]

In the present study, continuous welding of iron and copper using a laser heat source is investigated. The primary aim is to characterize the microstructure evolution in weldments of a binary couple of pure metals and to delineate the unique features that need understanding. This article highlights the microstructural features that are different from the welding of similar metals/alloys. A qualitative rationalization of the observed features using thermodynamic concepts as well as mass transport has also been attempted in this article.

II. EXPERIMENTS

Iron and copper of high purity (99.99 pct) are taken in the form of bars of a square cross section (7 × 7 × 60 mm) and clamped in a butt-weld geometry after a careful polishing and facing operation. A high-power (5.5 kW) CO_2 laser is used, with a welding-head focal distance of 152.4 mm. An inert-gas shroud containing a mixture of helium and argon is used as a protective atmosphere for all the experiments. The laser is precisely positioned using a ruby laser before each experiment to ensure that the power distribution is symmetrical to the parting line of the dissimilar couple. The actual power is calibrated after each set of experiments using a power meter. The sample is traversed at speeds varying from 8 to 169 mm/s using a numerically controlled table to obtain continuous welds. The power distribution is varied using different levels of defocus (the focus lies above the surface) which lead to different beam diameters. Welding is carried out under several conditions ranging from keyhole-mode welding to conduction-mode welding to determine the microstructural features that are independent of welding mode. Of these, three conditions have been chosen to present the results and are listed in Table I. The three conditions will be referred to henceforth as samples A through C. Samples A and B correspond to keyhole-mode welding with focused and defocused beams, respectively. Sample C corresponds to conduction-mode welding.

The welds obtained in the present study are all free of cracks. The weld samples are sectioned perpendicular to the welding direction for characterization. The samples are differentially etched with 4 pct Nital on the iron side and weld region and with $K_2Cr_2O_7$ solution on the copper side to reveal the entire microstructure across the weldment. The microstructure is analyzed using optical microscopy; scanning electron microscopy (SEM) using both a field-emission-gun (FEG) microscope as well as a standard microscope; and transmission electron microscopy (TEM). Compositions at various locations are determined using an energy-dispersive X-ray analyzer attached to the scanning electron microscopes. Thin discs of 3 mm in diameter are punched from the top, middle, and the bottom of weldments and are thinned using an ion mill to prepare samples for transmission electron microscope studies. The microhardness is also used as a probe to supplement microstructural observations as well as to obtain some preliminary assessment of the mechanical properties. A load of 25 gm and a diamond pyramid indenter are used for the hardness measurements.

Table I. Processing Conditions

	Power (kW)	Beam Diameter (mm)	Traverse Speed (mm/s)
Sample A	5.5	0.5 (focus)	21
Sample B	5.5	2.0 (defocus)	21
Sample C	4.5	2.0 (defocus)	25
Gas shroud		Ar + 30 vol pct He, 8 cm^3 s^{-1}	
Laser		Trumpf cw-CO_2	
Laser optics		Zeiss head, focal length 6 in.	
Power calibration factor		0.788	

III. RESULTS

A. *Weld-Pool Shape*

Figures 2(a) through (c) show the weld-pool shapes for the three conditions under study. While Figures 2(a) and (b) show weld pools in keyhole-mode welding, Figure 2(c) shows the weld pool in conduction-mode welding. As the laser scanning velocity is increased, the weld-pool dimensions decrease (Figure 2(d)). With an increasing traverse speed, the depth decreases more rapidly compared to the width. In all cases, the weld-pool shape is asymmetric about the centerline of the weld. More iron as compared to copper melts for all the processing conditions. The asymmetry is more significant at higher traverse speeds. One can also notice microstructural banding in the weld pool. The weld interface on the iron side is smooth, while that on the copper side appears jagged.

B. *Interface Microstructure*

The microstructure of the fusion zone near the weld interface on the iron side is shown in Figure 3. As can be seen in Figure 3(a), the weld interface on the iron side is smooth, with some of the favorably oriented iron grains growing into the weld. Further, at the initial stage, the growth occurs without any intercellular segregation, suggesting growth due to a thermal field only. However, beyond a small distance (2 to 3 μm from the interface), a cellular microstructure with partitioning in the intercellular region emerges. The further growth occurs in this cellular mode for the rest of the weld.

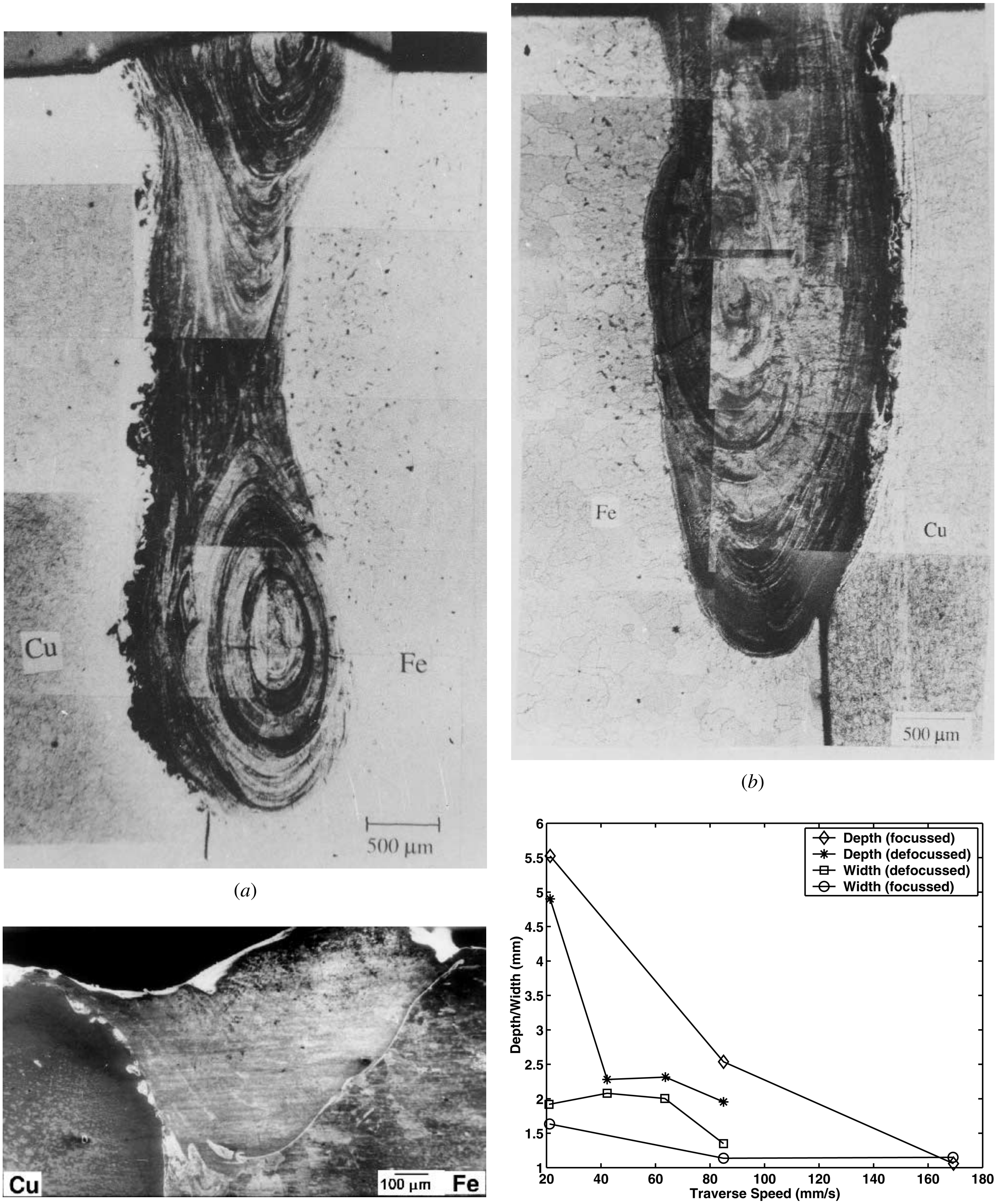

(*a*) (*b*) (*c*) (*d*)

Fig. 2—Low-magnification micrographs showing complete pool shapes for (*a*) sample A, (*b*) sample B, (*c*) sample C, and (*d*) the variation of the magnitudes of the width and depth of the weld pool.

The composition (Figure 3(b)) shows a gradual increase in the copper content from the base metal into the weld. A characteristic feature of the growth is the existence of distinct microstructural bands. These bands are characterized by a change in the microstructural length scale (size of the cells) as well as composition (Figure 3(b)). The fluctuations in

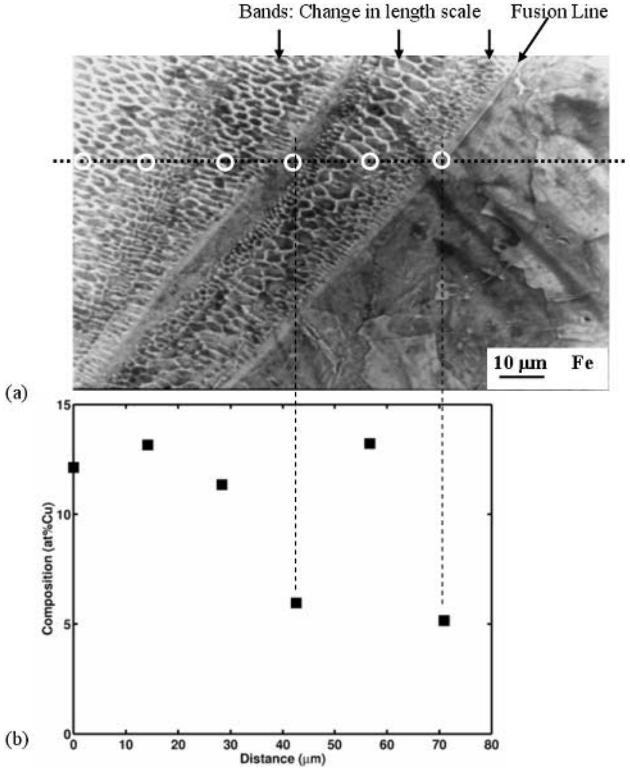

Fig. 3—(*a*) The microstructure at the iron interface of the weld for sample C and (*b*) the corresponding composition profile. The white circles indicate the locations where compositions are measured. Dashed lines are added as a guide for the eye. The length scale is the same as in the image and starts from the left-hand side of the image.

composition, however, are observed to be small, such that the weldment near the iron interface is always iron-rich.

The microstructure near the interface on the copper side is more complex. The interface itself is macroscopically rough (Figure 2) and is found to be so at all the processing conditions. The copper grains of the base metal apparently do not grow into the weld. The interface appears jagged, and the extent of fusion is not clear. Upon careful etching, it is observed that the extent of fusion on the copper side is different from the jagged interface (Figure 4(a)). The latter marks a separation of the regions where distinct mixing of the elements has taken place and the regions that are essentially copper. The lack of mixing on the copper side and the mixed region at the interface is clear in Figure 4(a). Compositional analysis as a function of distance away from the base metal (Figure 4(c)) shows that, ahead of the copper grains, a band of nearly pure iron exists (Figure 4(b)). The change in composition across the bands is much larger than that on the iron side. These bands are qualitatively different from those within the weld and near the iron interface.

C. *Weld Microstructure*

The microstructure of the weldments contains two distinct features. These are a fine cellular structure and a curved banded structure resembling a convective cell. The location of this feature depends on the welding conditions. Henceforth, it will be referred to as the "weld eye". The microstructure is observed to be cellular throughout the weldment and remains qualitatively the same across a range of processing conditions. In most cases, cells are fine and vary between 1 and 6 μm in size. A TEM analysis of the weldment is carried

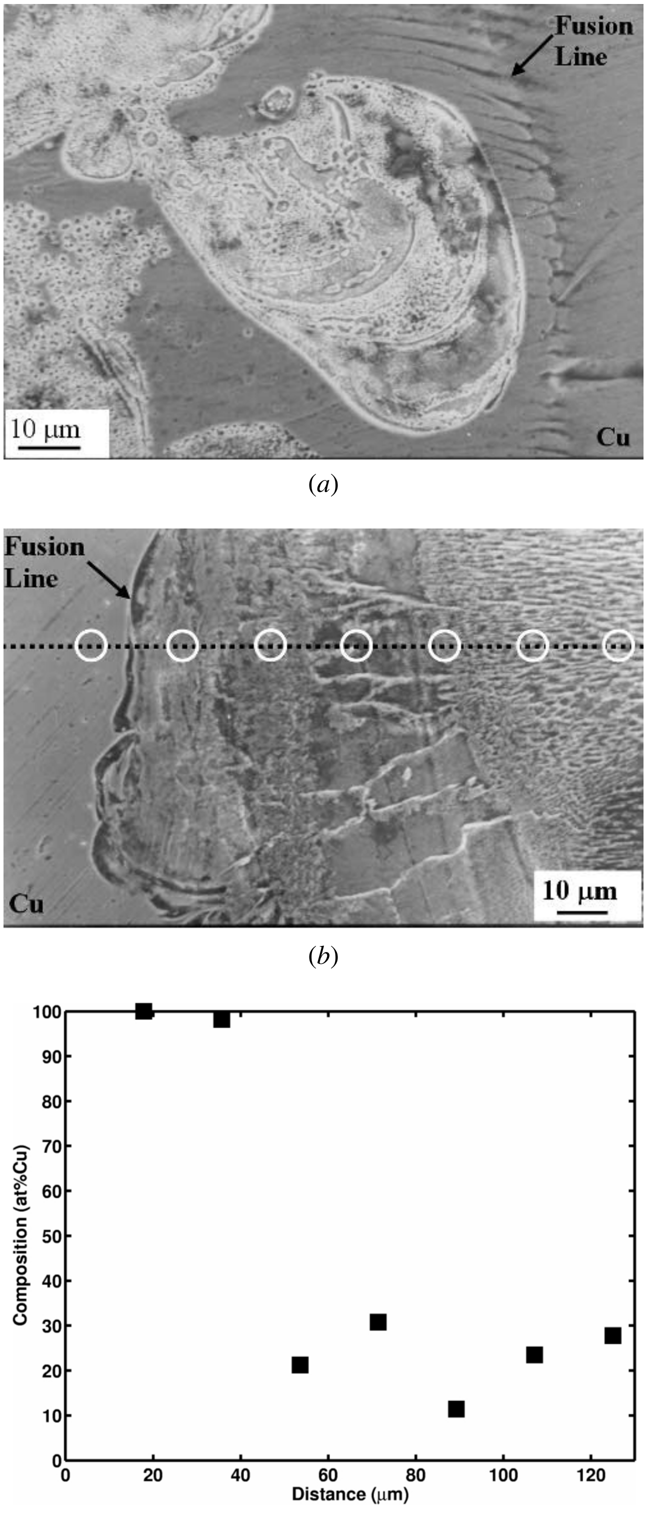

(*a*)

(*b*)

(*c*)

Fig. 4—The microstructure at the copper interface of the weld for (*a*) sample B and (*b*) sample C. (*c*) The composition profile corresponding to (*b*). The white circles indicate the locations where compositions are measured. The length scale is the same as in the image and starts from the left-hand side of the image.

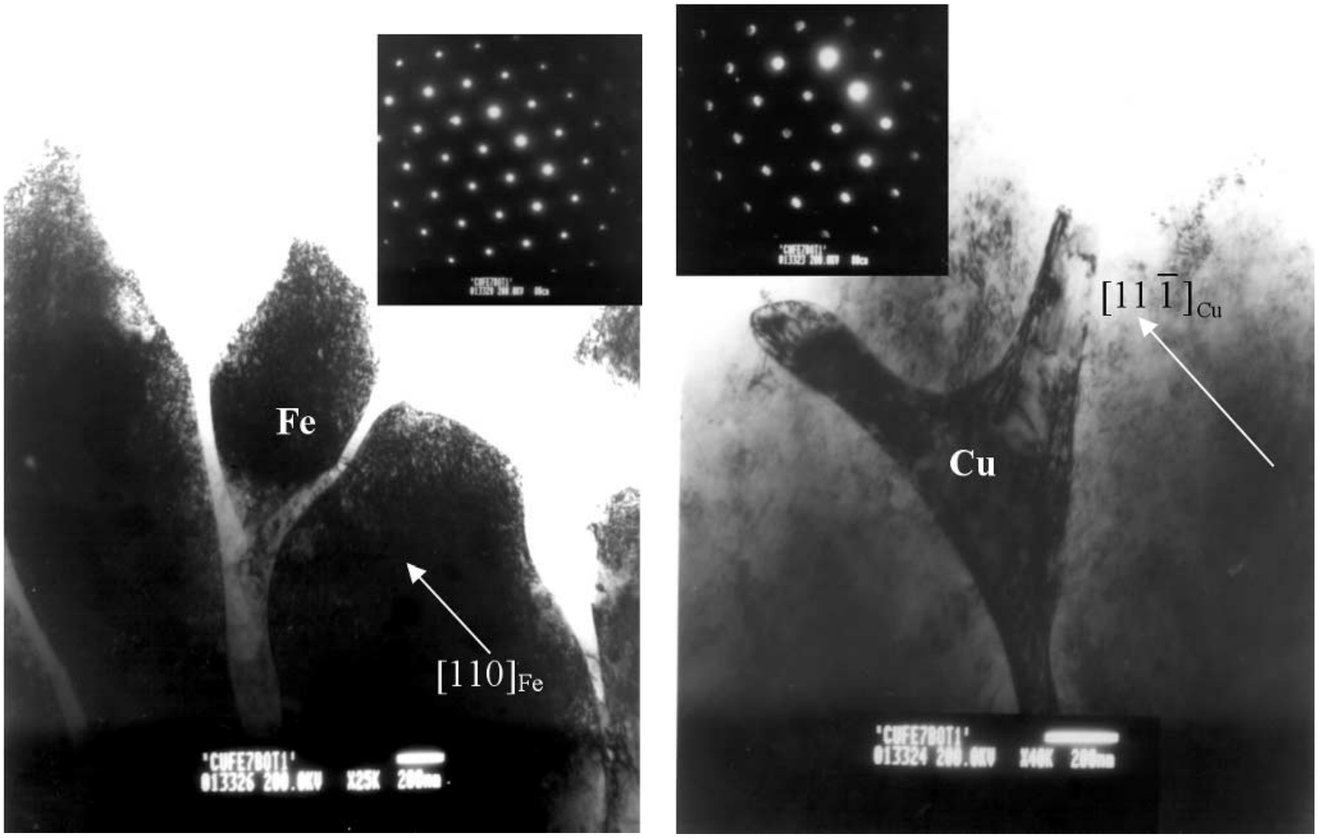

(*a*) (*b*)

Fig. 5—Bright-field images showing (*a*) cellular iron grains ($[\bar{1}11]$ zone) and (*b*) intercellular copper ([011] zone).

out to reveal the nature of the microstructure in detail. A set of bright-field images and the corresponding selected-area diffraction patterns of the cellular region and the complementary intercellular region are shown in Figures 5(a) and (b). The intercellular regions contain fcc copper, while the cellular grains are composed of bcc iron. The cellular grains of iron are about 1 μm in size, and the intercellular copper has a thickness of about 0.2 μm. Superposition of the two diffraction patterns indicates that the orientation of the copper in the intercellular region is close to the Kurdjomov–Sach orientation relation given by $[011]_{Cu} /\!/ [\bar{1}11]_{Fe}$ and $(11\bar{1})_{Cu} /\!/ (110)_{Fe}$. The deviation in this case is 2.5 deg.

In addition to the aforementioned features, one observes tiny dots in the microstructure when imaged in the FEG SEM apparatus. This is shown in Figure 6(a). The TEM investigation reveals these isolated globular droplets of iron as well as copper in the weld region. Figure 6(b) shows a bright-field image in the $[\bar{1}12]$ zone of fcc copper taken at the middle of the weld pool, showing copper droplets in the iron matrix. A selected-area diffraction pattern taken from the corresponding region is shown in Figure 6(c). The extra reflections marked in the pattern are identified to be from the surrounding iron matrix. The [110] reflection of Fe is 10.5 deg away from the [111] reflection of copper. Analysis of this and other patterns reveals that the orientation relationship is again given by the Kurdjumov–Sach relationship.

In general, the microstructural banding can be observed throughout the middle regions in the weldments. The scale of the cellular pattern inside the bands, however, does not change significantly in these bands. Figures 7(a) and (b) show a typical micrograph and the composition profile across the bands. The composition is taken from an area (5×5 μm) such that the composition change from a cell to intercellular region is avoided. As can be seen, the composition in the interband region is significantly iron-rich compared with the interior of the band.

The banding observed near the eye of the weld pool needs special attention. The bands form the weld eye at the center of the weld pool for conduction-mode welds and form two weld eyes, at the top and bottom, for keyhole-mode welds. A detailed microstructure of these bands is shown in Figure 7(c). The low-magnification micrograph of a portion of the weld eye is shown in the inset, while the microstructure at a higher magnification is shown in the main Figure 7(c). The microstructural bands are characterized by change in composition as well as the length scale of the cellular pattern. The weldment microstructure away from the weld eye is shown in Figure 7(d) for comparison with Figure 7(c).

D. *Mechanical Characterization*

Hardness measurements are carried out both as a probe for the microstructure as well as to give an idea of the mechanical properties. Sets of detailed hardness measurements as a function of spatial coordinates in the weld pool are carried out for the keyhole-mode welds in both the focused- and defocused-beam conditions (Figures 2(a) and (b)). Hardness values are taken at several locations across

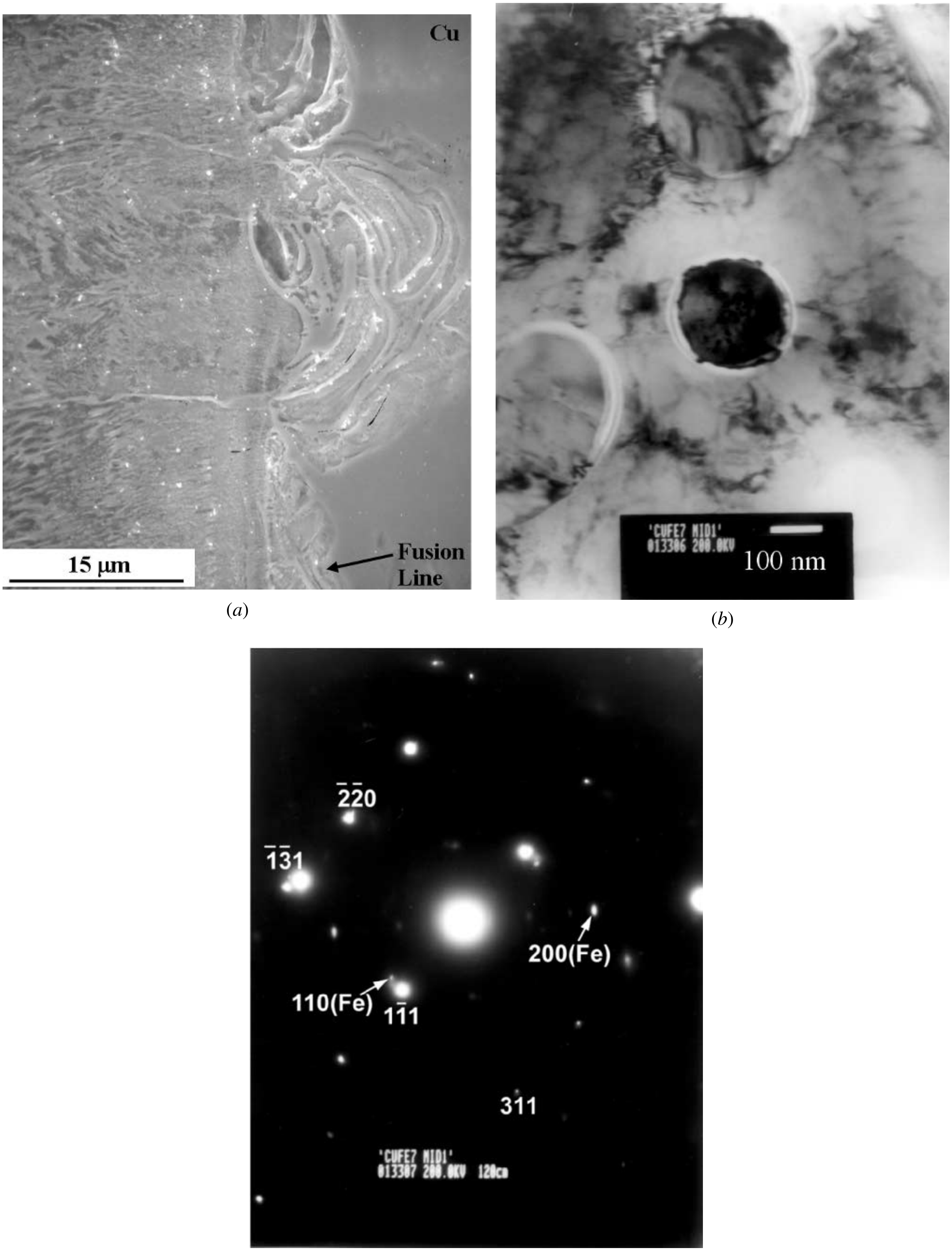

(*a*) (*b*) (*c*)

Fig. 6—The microstructure of weld for sample B. (*a*) FEG SEM image of the copper interface, showing globules of copper (white). (*b*) At the middle of the pool, a bright-field image in the [$\bar{1}12$] zone showing a copper globule in the iron matrix and (*c*) the corresponding selected-area diffraction pattern.

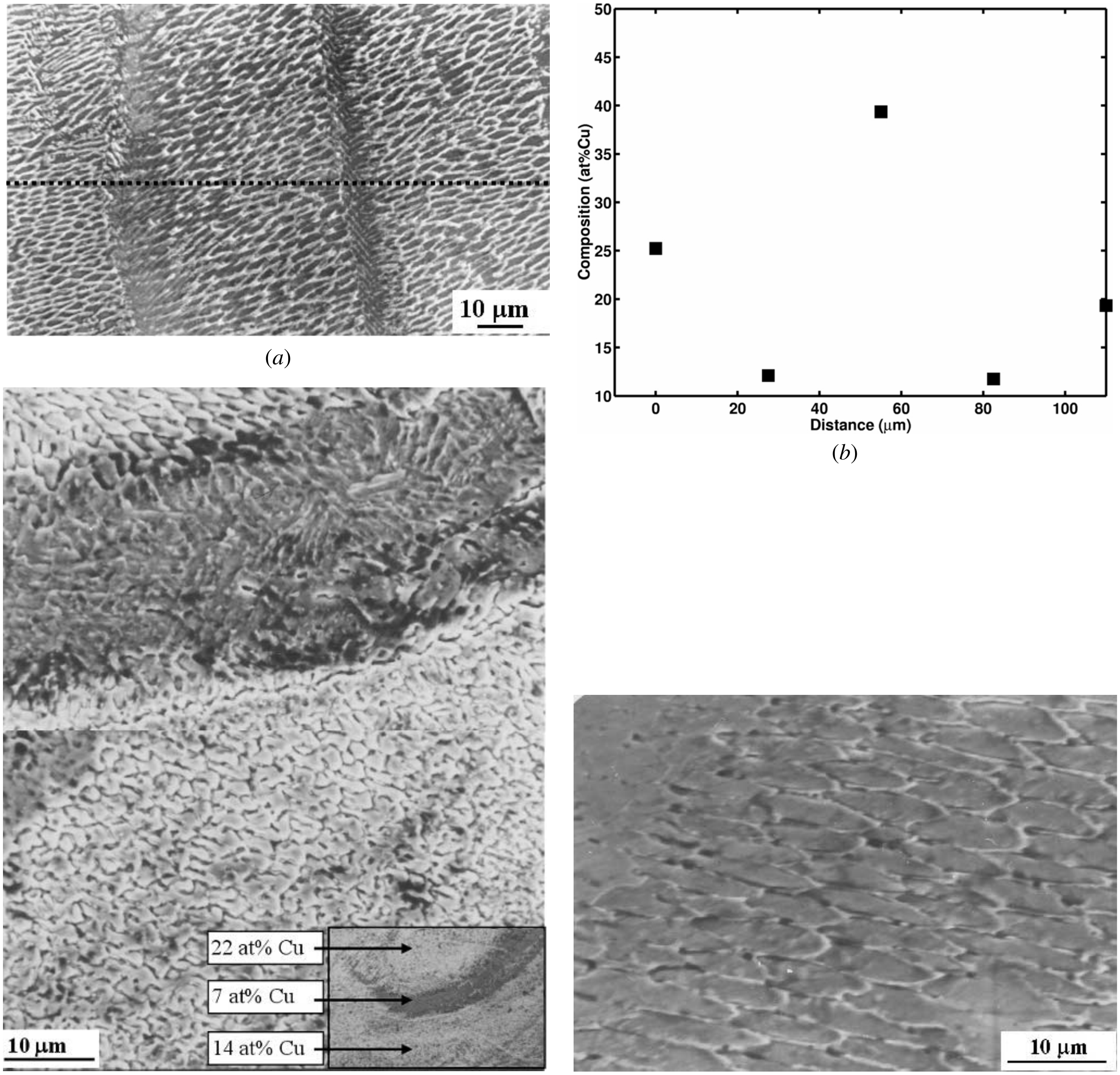

(*a*) (*b*) (*c*) (*d*)

Fig. 7—(*a*) Microstructural banding and the corresponding (*b*) composition analysis for sample C. (*c*) The microstructure at the center of the vortex for the weld pool (sample B). The inset shows the microstructure at the vortex at a lower magnification, with compositions across the bands. (*d*) The microstructure of the weld near the iron interface (sample B).

the weld and at different heights to form an array of points covering the entire weldment. The values are then plotted using a contour map and superimposed with the weld-pool shape (shown in bold) in Figures 8(a) and (b). The hardness values are indicated by the VHN as contour labels. While the spatial resolution of the hardness measurements and the lack of a corresponding composition map limit a direct comparison of the hardness map with the weld micrograph, one can nevertheless notice certain correlations with the microstructures shown in Figures 2(a) and (b). There is a distinct increase in hardness in the weldment, and it is noticed usually where there is banding. The highest hardness can be identified to be where the microstructural length scale is the finest.

IV. DISCUSSION

A. *Weld-Pool Shape*

The shape of the weld pool is altered by the laser power and scanning rate because of a change in the welding mode. The change of mode from conduction to keyhole alters the absorption of the laser intensity along the depth of the pool and changes the depth more significantly than the width.

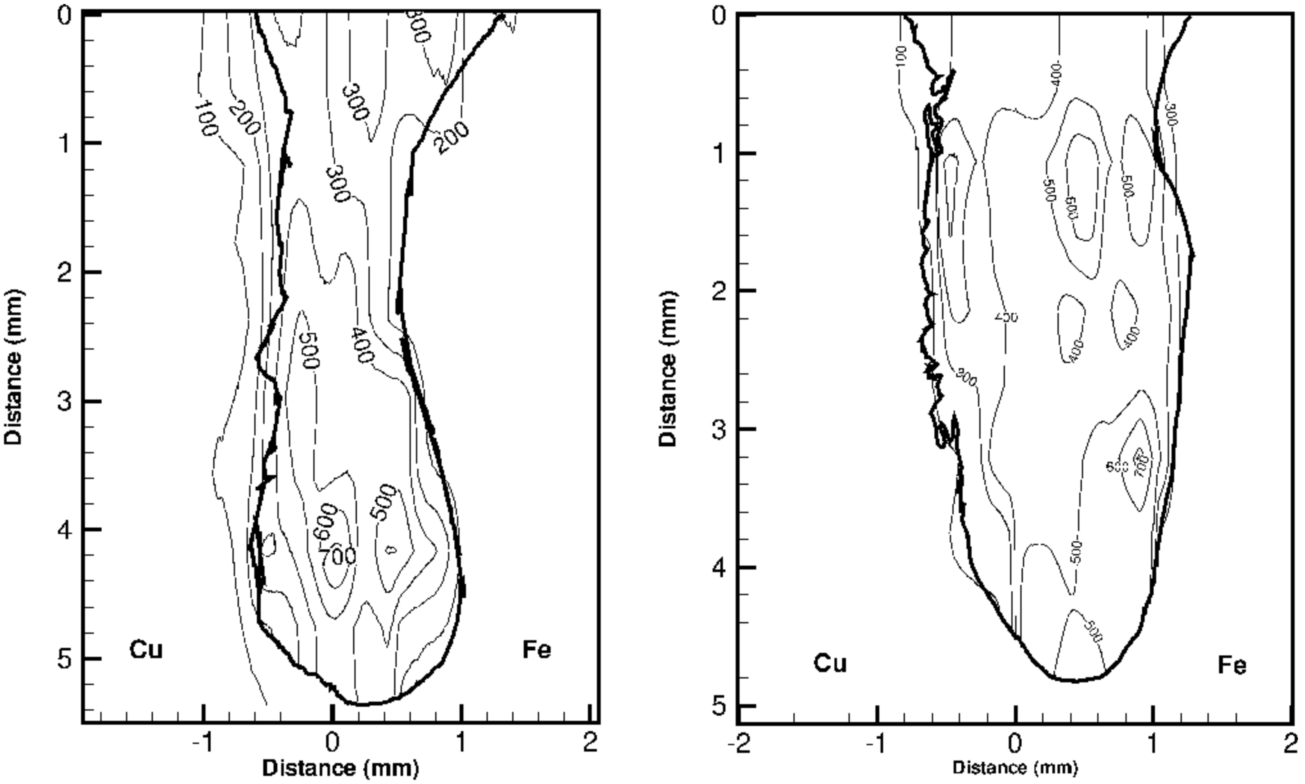

(*a*) (*b*)

Fig. 8—Hardness maps of the weld for (*a*) sample A and (*b*) sample B. The weld-pool shape is superimposed on the contours using bold lines. Hardness values (in VHN) are shown as contour labels.

The shape of the keyhole is also different when the laser-power distribution is changed. The present understanding of the keyhole formation is inadequate to extend it directly to dissimilar couples.

A computational model for the conduction-mode laser welding of the dissimilar joints developed earlier by the authors and applied to the case of a copper-nickel couple[19] could be used here. The thermophysical properties of iron are similar to those of nickel. Hence, the understanding derived from the computational results for the evolution of the weld-pool shape during laser welding of copper-nickel could also be extended to the current system. For a detailed simulation showing the evolution of the temperature field, convection profile, and composition gradients, the reader is referred to an earlier work.[19] Due to its lower thermal diffusivity, for a symmetric distribution of the laser heat source, the iron side has more sensible heat than the copper side. Thus, iron melts first and solidifies last, leading to a greater amount of molten iron than copper. Transport of heat to the copper side is mainly due to Marangoni convection of liquid in the weld pool, rather than by direct heating. When the laser moves off, due to its high thermal diffusivity, the copper side solidifies first. Thus, the time spent by the iron side in the liquid state is about an order of magnitude longer than that spent by the copper side. Mixing by convection is unequal on the two sides, leading to a well-mixed iron-rich region on the iron side and a copper-rich region with a high compositional gradient on the copper side of the weld pool.[17] The asymmetric weld-pool shape and composition profile are also a direct consequence of this process. At low welding speeds, such a heat transport would lead to a decrease in the asymmetry of the weld-pool shape, as is also observed in the experiments.

B. *Interface Microstructure*

The apparent lack of homogeneity in the weld microstructure and complex features such as microstructural banding preclude a simplistic analysis to rationalize all the experimental observations. In this section, growth of pure-metal grains from the base metals on the two sides into the alloy liquid in the weld pool is considered. It will be shown that upon undercooling, grains from the iron side can grow into the weld pool, but such a possibility does not exist for grains from the copper side.

The growth rate of the solid during laser processing is related to the laser-scan velocity.[29] The interface velocity required for nonequilibrium effects such as solute trapping from liquid for most metallic solid solutions is of the order of few meters/second.[30] These velocities are significantly higher than the laser-scan speeds used in the present study. Hence, the assumption of the local equilibrium at the solidification front is reasonable. A thermodynamic analysis to explain the difference in the microstructural features at the weld/base-metal interface is presented subsequently. Two situations are considered: that of the weld/iron interface and that of the weld/copper interface, respectively.

For illustration, the alloy liquids are assumed to be Fe + 10 at. pct Cu ahead of the weld/iron interface and Cu + 10 at. pct Fe ahead of the weld/copper interface. The compositions of the liquids chosen for the analysis are widely different on the two sides of the weld, as discussed in Section IV–A. From the overall compositions taken at various locations in the weld (*e.g.*, Figures 3(b) and 4(c)), these compositions are reasonable to use to analyze the basic features of the nature of the solidification. However, the conclusions of the analysis do not change with the composition of the liquid metal ahead of the base metal, as long as the base metal is pure. Thermodynamic data are obtained from the latest compilation of existing thermodynamic data that accurately reproduce the equilibrium and metastable phase boundaries in the iron-copper system.[31]

Consider the case of an Fe + 10 at. pct Cu alloy liquid (C_L) ahead of the pure-iron base metal. The free-energy curves for the Fe-Cu binary system at a temperature of 1765 K are shown in Figure 9(a). The common tangent construction between the liquid and Fe free-energy curve gives the composition of iron solid solution (C_S) in equilibrium with the alloy liquid ahead of the interface at this temperature. Thus, any liquid with a composition between C_S and C_L can partition in an equilibrium manner between the two compositions of solid and liquid. In the present case, the molten weld pool with the given liquid composition, which has evolved due to convective mixing of the melt of pure components (Fe-10 pct Cu, in our example), is in contact with the pure-iron base metal. As can be seen from the curve, the iron substrate cannot grow into the melt. In this situation, solidification can take two paths. One is by homogeneous nucleation of a solid-solution grain in the melt, of a composition compatible with that of the liquid. In the absence of this event, the liquid will follow a path dictated by the local thermodynamic conditions. As indicated by the intercepts on the *y*-axis of tangents from the free-energy curves, the chemical potential of pure iron (μ_0) is higher than that of the solid solution (μ_1), which is in equilibrium with the liquid. Due to the difference in the chemical potential of the Fe atoms, they can jump from the Fe base metal to the liquid, effecting a melting. However, copper in the alloy liquid has higher chemical potential than copper at the iron base metal near the interface and, thus, can promote the process of alloying of the iron base-metal grains at the interface, with copper atoms jumping from the liquid to the base metal. Since solidification cannot take place at this temperature, the high heat-transfer rate through the base metal will lead to further undercooling, reducing the difference in chemical potential. Thus, there will be a process of increasing undercooling and increasing copper content at the iron base-metal/liquid interface until local equilibrium is established. Growth of the substrate into the melt will then take place at this lowered temperature (undercooled condition). Thus, the appearance of continuous growth of the iron grain into the weld can be rationalized.

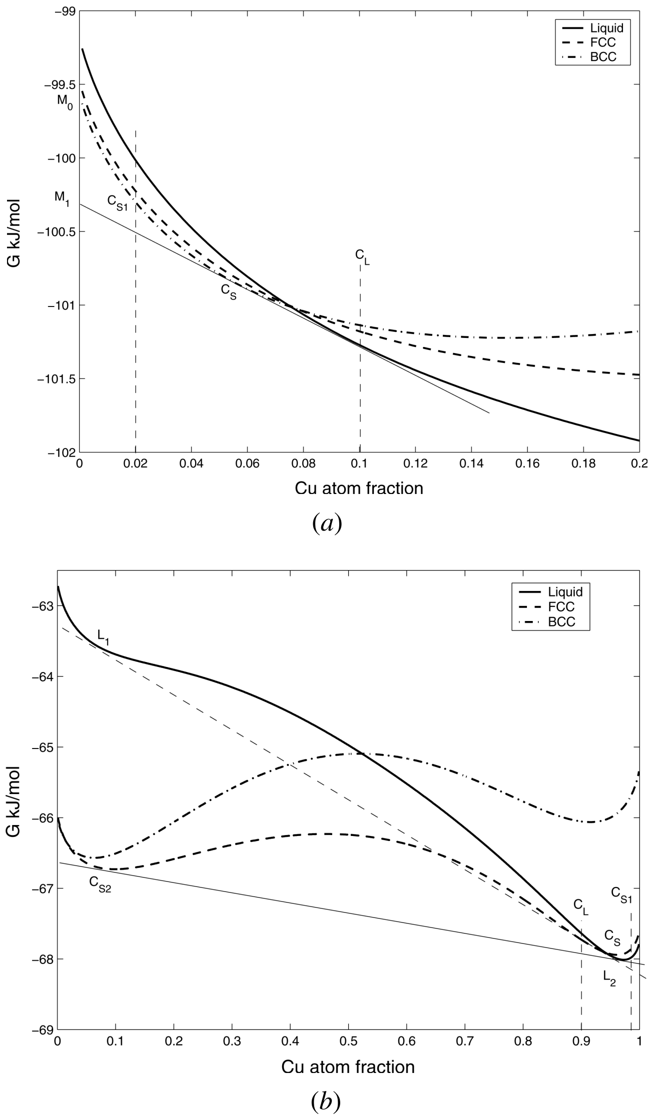

(*a*)

(*b*)

Fig. 9—Gibbs free-energy curves for the iron-copper system calculated at (*a*) 1765 K and (*b*) 1375 K.

Let us now consider the case of the Cu + 10 at. pct Fe alloy liquid ahead of the pure-copper base metal. The free-energy curves for a temperature of 1375 K are shown in Figure 9(b). It is clear, also from the phase diagram, that no solid solution of copper is thermodynamically stable above the peritectic temperature (1367 K). However, an iron-rich solid of the composition C_{S2} can precipitate from the alloy liquid. Since nucleation of iron phase will require the alloy melt to undercool, metastable liquid-phase separation can also take place.

Once the iron-rich solid forms in the melt, copper-rich solid can also form *via* a peritectic reaction. The experimental observation in Figure 4, showing iron-rich and copper-rich regions in alternating bands ahead of the pure-copper base metal, supports the aforementioned rationalization. On the copper side, one can clearly see the microstructural difference between the alloyed region due to convective mixing and the region where pure copper has been solidified by the regrowth of the copper base metal (Figure 4(a)). The fine bands observed near the Cu interface (Figures 4(b) and 6(c)) are qualitatively different in appearance and much finer than the bands (ripples) observed in the weld pool. These alternating bands, with large jumps in composition from nearly pure iron to nearly pure copper, show the signature of a peritectic reaction. The alloy liquid can solidify only after the iron precipitation has occurred, and, therefore, the solidification can occur only from the melt. Thus, the interface microstructure is different on the copper side as compared to the iron side.

C. *Weld Microstructure*

Microstructural bands are observed to be parallel to the weld/base-metal interface. The appearance of these converging bands is similar to what are commonly referred to as weld ripples.[32] Unsteady growth of the solidification interface during laser welding has recently been observed using a high-speed camera technique.[33] Vigorous convection due to laser-induced Marangoni forces in the weld pool and the moving solidification front can lead to fluctuations in the temperature and composition of the alloy liquid ahead of the solidification front. The cellular mode of growth can change from coarse cells to fine cells to dendrites, corresponding to the changes in growth conditions such as an increase in velocity, decrease in temperature gradient, *etc*.[34] Since the partitioning of solute is predominantly in the lateral direction for fine cells, one expects a higher concentration of (intercellular) copper in such a region. When the solidification is with coarse cells, the solute-rich liquid is swept ahead in the direction along the growth, leading to solute-depleted regions behind. The bands are, therefore, likely due to fluctuations in the growth conditions leading to such fluctuations in cell spacing and composition ahead of the solidification front.

The undercooling required for iron-copper alloy liquids to exhibit liquid-phase immiscibility was calculated earlier as a function of composition.[24,25] For an ~50 at. pct composition, the undercooling required for liquid-phase separation is only 17 K.[24] Earlier experimental studies on the submerged miscibility gap in iron-copper melts[28,35,36] demonstrate the ease of accessing the miscibility gap. Figure 9(b) also illustrates the possibility of the alloy liquid separating into two liquids (L_1 and L_2) due to the submerged miscibility gap. Experimental observations (Figure 6) indicate that such a phase separation has also occurred during the weld solidification. The presence of isolated globular grains of iron as well as copper in the weld region suggest that during the solidification of the weld pool, the liquid alloy undergoes a certain extent of undercooling. However, it is difficult to quantify this undercooling in the absence of a direct observation of the time-resolved temperature distribution in the weld region during weld solidification.

D. *Mechanical Behaviour*

The outline of the weld-pool shape (Figures 8(a) and (b)) is compared with the corresponding microstructures (Figures 2(a) and (b)) to note that the peak in hardness occurs where the microstructure in the bands is fine. Figures 7(c) and (d) show weld microstructures taken at the center of the weld eye and near the iron interface, respectively. The spacing of cellular patterns at the weld eye is much finer than that near the interface. From the microstructure, it is also seen that at the middle of the pool, there are several microstructural bands with alternating layers of iron-rich and copper-rich regions. The increased hardness near the center of the weld can possibly be due to the fine scale of the microstructure at the location. The microstructure in the bands consists of cellular grains of iron with intercellular copper. In order to determine whether such a fine scale of microstructure with alternating layers of iron and copper can lead to strengthening, a modified Hall–Petch relation is used.

The ratio of the widths of cellular grains of iron to the intercellular copper is 5:1 (Figure 5). Shingu *et al.*[37] studied the applicability of the Hall–Petch relation to explain the increase in hardness of Fe/Cu multilayers and found that, for a layer thickness greater than 35 nm, the rule of mixtures is followed, as given subsequently:

$$\sigma = \sigma_{\mathrm{Fe}} V_{\mathrm{Fe}} + \sigma_{\mathrm{Cu}} V_{\mathrm{Cu}} \qquad [1]$$

$$\sigma_X = \sigma_{0,X} + k_X d^{-0.5} \qquad [2]$$

where the subscript X refers to Fe and Cu; V_{Fe} and V_{Cu} are the volume fractions of iron and copper, respectively; σ is the hardness, d is the size of layer in nm; $\sigma_{0,\mathrm{Fe}}$ = 2.02 GPa; $\sigma_{0,\mathrm{Cu}}$ = 0.377; k_{Fe} = 16.4 GPa$\sqrt{\mathrm{nm}}$; and k_{Cu} = 2.95 GPa$\sqrt{\mathrm{nm}}$. Let us consider that the alternating regions of iron (as cells of ~1 μm in size) and copper (as intercellular regions of ~0.2 μm in size) in the cellular microstructure as similar to Fe/Cu multilayers of an equivalent layer thickness. These length scales are within the range of applicability of the Hall–Petch relation with the rule of mixtures. Using the volume fraction of iron to copper of 5:1 and a factor of 3 to convert the hardness in VHN to strength in MPa, Eqs. [1] and [2] give the hardness as 740 VHN. This value is close to the peak hardness found experimentally. While the quantitative accuracy is not critical in this case, the estimate shows that the fine scale of the cellular microstructure gives rise to a high hardness of the weldment. Thus, the improved hardness in the Fe-Cu dissimilar weld could be explained as being due to the fine microstructure of alternating iron and copper acting as a multilayer.

V. CONCLUSIONS

1. Iron and copper are welded without cracks using a high-power continuous CO_2 laser.
2. The weld-pool shape is asymmetric at all the traverse speeds.
3. The microstructure is different at the two weld/base-metal interfaces. Grains of iron substrate grow into the weld, whereas on the copper side, the solidification occurs from the melt pool with the formation of iron-rich bands.
4. The weld microstructure inside the weld pool is predominantly cellular and characterized by microstructural banding with concurrent fluctuations in composition.
5. Evidence is also presented to show that, occasionally, the melt in some local regions has undergone a liquid-phase separation due to a submerged miscibility gap.
6. A thermodynamic rationalization is proposed to explain the difference in interface microstructure on the two sides of the weld.
7. The hardness of the weld region is higher than that of the base metals. The alternating fine regions of iron and copper in the weld lead to higher hardness. This can be rationalized by invoking a Hall–Petch type of model for the strength of the multilayer, employing a rule of mixing.

ACKNOWLEDGMENTS

The authors thank Rolf Galun, Scientist, IWW, Technical University–Clausthal for some of the experimental facilities. The work derives support from the Indo–United States Project No. ONR N00014-95-1-0073. The authors thank the reviewers for many constructive suggestions.

REFERENCES

1. W.M. Steen: *Laser Material Processing*, Springer-Verlag, New York, NY, 1991.
2. W. Duley: *Laser Welding*, John Wiley & Sons Inc., New York, NY, 1999.
3. P.S. Wei and F.K. Chung: *Trans. ASME: J. Heat Transfer*, 1997, vol. 119, p. 832.
4. P.J. Blakeley and A. Sanderson: *Welding J.*, 1984, vol. 63, pp. 42-49.
5. P.S. Wei and Chih-Wei Wen: *Metall. Mater. Trans. B*, 2002, vol. 33B, pp. 765-73.
6. O.K. Nazarenko: *Avt. Svarka*, 1982, No. 1, pp. 33-39.
7. S.A. David and J.M. Vitek: *Int. Mater. Rev.*, 1989, vol. 34, pp. 213-45.
8. T. Zachariah, S.A. David, J.M. Vitek, and T. Debroy: *Welding Res. Suppl.*, 1989, Dec., pp. 499s-509s.
9. T. Zachariah, S.A. David, J.M. Vitek, and T. Debroy: *Welding Res. Suppl.*, 1989, Dec., pp. 510s-519s.
10. Z. Sun and J.C. Ion: *J. Mater. Sci.*, 1995, vol. 30, pp. 4205-15.
11. J. Seretsky and E.R. Ryba: *Welding Res. Suppl.*, 1976, July, pp. 208s-211s.
12. G. Metzger and R. Lison: *Welding Res. Suppl.*, 1976, Aug., pp. 230s-240s.
13. B. Majumdar, R. Galun, A. Weisheit, and B.L. Mordike: *J. Mater. Sci.*, 1997, vol. 32, pp. 6191-6200.
14. P.S. Wei, Y.K. Kuo, and J.S. Ku: *J. Heat Transfer–Trans. ASME*, 2000, vol. 122, pp. 626-31.
15. Z. Li and G. Fontana: *J. Mater. Processing Technol.*, 1998, vol. 74, pp. 174-82.
16. A.C. Lingenfelter: *Proc. Laser Advanced Materials Processing*, High Temperature Society of Japan, Welding Research Institute of Osaka University, Mihogaoka, Ibaraki, Osaka, Japan, 1987, pp. 211-16.
17. Gandham Phanikumar: Ph.D. Thesis, Indian Institute of Science, Bangalore, 2002.
18. G. Phanikumar, K. Chattopadhyay, and P. Dutta: *Int. J. Numer. Methods Heat Fluid Flow*, 2001, vol. 11 (2), pp. 156-71.
19. G. Phanikumar, P. Dutta, and K. Chattopadhyay: *Metall. Mater. Trans. B*, 2004, vol. 35B, pp. 339-50.
20. F.K. Chung and P.S. Wei: *J. Heat Transfer–Trans. ASME*, 1999, vol. 121, pp. 451-61.
21. P.S. Wei and F.K. Chung: *Metall. Mater. Trans. B*, 2000, vol. 31B, pp. 1387-1403.
22. *Binary Alloy Phase Diagrams*, T.B. Massalski, ed., ASM, Metals Park, OH, 1980.
23. S.P. Elder and G.S. Abaschian: *Proc. Principle of Solidification and Materials Processing*, R. Trivedi, J.A. Sekhar, and J. Mazumdar, eds., Oxford and IBH Publishing Co Ltd., New Delhi, 1989, vol. 1, pp. 1-299.
24. Y. Chuang, R. Schmid, and Y.A. Chang: *Metall. Trans. A*, 1984, vol. 15A, p. 1921.
25. Bhaskar Majumdar: Ph.D. Thesis, Indian Institute of Science, Bangalore, 1995.
26. A. Munitz: *Metall. Trans. B*, 1987, vol. 18B, pp. 565-75.
27. K.K. Prashanth, J. Mazumder, and K. Chattopadhyay: *J. Mater. Sci.*, 1999, vol. 34, pp. 3437-45.
28. K.S. Kumar, G. Phanikumar, P. Dutta, and K. Chattopadhyay: *J. Mater. Sci.*, 2002, vol. 37, pp. 2345-49.
29. M. Zimmermann, M. Carrard, and W. Kurz: *Acta Metall.*, 1989, vol. 37, pp. 3305-13.
30. D.M. Herlach: *Mater. Sci. Eng.*, 1994, vol. R12 (4–5), pp. 177-272.
31. Q. Chen and Z. Jin: *Metall. Mater. Trans. A*, 1995, vol. 26A, pp. 417-26.
32. S.A. David, J.M. Vitek, M. Rappaz, and L.A. Boatner: *Metall. Mater. Trans. A*, 1990, vol. 21A, pp. 1767-82.
33. P.S. Mohanty and J. Mazumder: *Metall. Mater. Trans. B*, 1998, vol. 29B, pp. 1269-79.
34. Billia and Trivedi: in *Handbook of Crystal Growth*, D.T.J. Hurle, ed., Elsevier, Amsterdam, 1993, vol. 1b, p. 899.
35. G. Wilde and J.H. Perepezko: *Acta Mater.*, 1999, vol. 47 (10), pp. 3009-21.
36. X.Y. Lu, C.D. Cao, and B. Wei: *Mater. Sci. Eng. A*, 2001, vol. 313, pp. 198-206.
37. P.H. Shingu, K.N. Ishihara, A. Otsuki, and I. Daigo: *Mater. Sci. Eng. A*, 2001, vols. 304–306 (1–2), pp. 399-402.